Trabid patient mutations impede the axonal trafficking of adenomatous polyposis coli to disrupt neurite growth

Daniel Frank[1,7,14], Maria Bergamasco[2,7,14], Michael Mlodzianoski[3,7,14], Andrew Kueh[4,7,8,9], Ellen Tsui[5,7], Cathrine Hall[6,7], Georgios Kastrappis[10], Anne Kathrin Voss[2,7], Catriona McLean[11], Maree Faux[12], Kelly Rogers[3,7], Bang Tran[10], Elizabeth Vincan[10,13], David Komander[1,7], Grant Dewson[1,7,15], and Hoanh Tran[1,7,10,15]

[1]Ubiquitin Signalling Division, [2]Epigenetics and Development Division, [3]Centre for Dynamic Imaging, [4]Melbourne Advanced Genome Editing Centre, [5]Histology Facility, [6]Inflammation Division, Walter and Eliza Hall Institute of Medical Research, Parkville, VIC 3052, Australia
[7]Department of Medical Biology, The University of Melbourne, Parkville, VIC 3052, Australia
[8]Olivia Newton-John Cancer Research Institute, Heidelberg, VIC 3084, Australia
[9]School of Cancer Medicine, La Trobe University, Heidelberg, VIC 3084, Australia
[10]Department of Infectious Diseases, The University of Melbourne at The Peter Doherty Institute for Infection and Immunity, Melbourne, VIC 3000, Australia
[11]Department of Anatomical Pathology, The Alfred Hospital, Melbourne, VIC 3004, Australia
[12]Neuro-Oncology Group, Murdoch Children's Research Institute, Parkville, VIC 3052, Australia
[13]The Victorian Infectious Diseases Reference Laboratory, Royal Melbourne Hospital at The Peter Doherty Institute for Infection and Immunity, Melbourne, VIC 3000, Australia
[14]These authors contributed equally to this work
[15]Corresponding authors dewson@wehi.edu.au, tran.h@wehi.edu.au

Running Title: Deubiquitylating enzyme Trabid promotes polarised axon elongation

Abstract

Trabid/ZRANB1 missense mutations have been identified in children diagnosed with a range of congenital disorders including reduced brain size, but how Trabid regulates neurodevelopment is not understood. We have characterised these patient mutations in cells and mice to identify a key role for Trabid in the regulation of neurite growth. One of the patient mutations flanked the catalytic cysteine of Trabid and its deubiquitylating (DUB) activity was abrogated. The second variant retained DUB activity, but failed to bind STRIPAK, a large multiprotein assembly implicated in cytoskeleton organisation and neural development. *Trabid/ZRANB1* knock-in mice harbouring either of these patient mutations exhibited reduced neuronal and glial cell densities in the brain and a motor deficit consistent with fewer dopaminergic neurons and projections. Mechanistically, both DUB-impaired and STRIPAK-binding-deficient Trabid variants impeded the trafficking of adenomatous polyposis coli (APC) to microtubule plus-ends. Consequently, the formation of neuronal growth cones and the trajectory of neurite outgrowth from mutant midbrain progenitors were severely compromised. We propose that STRIPAK recruits Trabid to deubiquitylate APC, and that in cells with mutant Trabid, APC becomes hyperubiquitylated and mislocalised causing impaired organisation of the cytoskeleton that underlie the neuronal and developmental phenotypes.

Introduction

Deubiquitylating enzymes (DUBs) are integral components of the ubiquitin system that control protein functions essential for healthy development and aging (Clague et al. 2019). DUBs catalyze the removal of ubiquitin from protein substrates to regulate protein stability, activity, interaction, or localisation (Komander et al. 2009). Ubiquitin can be assembled into polymers linked through one of eight internal ubiquitin residues – Met1, Lys6, Lys11, Lys27, Lys29, Lys33, Lys48 and Lys63 – and impairment of DUB function can lead to the accumulation of one or more of these ubiquitin chain linkages on a protein substrate with deleterious consequences. For example, LINKage-specific deubiquitylation deficiency-induced Embryonic Defects (LINKED), a human syndrome caused by loss-of-function mutations in the DUB OTUD5, is associated with increased Lys48-linked ubiquitylation and turnover of chromatin remodeling and transcription factors that are critical for normal embryonic development (Beck et al. 2021).

63 Consequently, LINKED syndrome patients manifest severe congenital malformations and die in
64 early infancy (Beck et al. 2021). OTUD5 belongs to a 17-member family of human DUBs that
65 possess an OTU (*o*varian *tu*mour) catalytic domain and include the closely related OTU DUBs
66 A20, Cezanne and Trabid. Trabid missense mutations have been identified in children diagnosed
67 with a range of developmental disorders including microcephaly (Deciphering Developmental
68 Disorders 2015).
69
70 Trabid has two defining biochemical features. First, it exhibits strong DUB specificity for Lys29-
71 and Lys33-linked ubiquitin chains, cleaving these chain types 40-fold more efficiently than
72 Lys63-linked chains (Licchesi et al. 2012). Lys29-linked polyubiquitin exists mainly as
73 heterotypic chains containing Lys48 linkages that target substrates for degradation (Kristariyanto
74 et al. 2015; Leto et al. 2019; Harris et al. 2021). Trabid is thought to modulate the levels of
75 Lys29/Lys48 mixed chains to regulate proteostasis, autophagy and cell division (Chen et al.
76 2021; Yu et al. 2021; Vaughan et al. 2022). Lys33-linked ubiquitin polymers have been
77 implicated in post-Golgi protein trafficking (Yuan et al. 2014), and Lys63-linked chains are
78 abundant cellular adducts with established roles in the sorting of endosomal/lysosomal cargo
79 (Erpapazoglou et al. 2014) and mediating the formation of protein assemblies (Tran and Polakis
80 2012). The second defining feature of Trabid is that it binds the Striatin-interacting phosphatase
81 and kinase (STRIPAK) complex (Sowa et al. 2009; Tran et al. 2013; Harris et al. 2021), a large
82 multiprotein assembly implicated in cytoskeleton organisation, cell migration and neural
83 development (Hwang and Pallas 2014; Sakuma et al. 2014; Madsen et al. 2015; Bazzi et al.
84 2017; Kuck et al. 2019).
85
86 We have previously identified the adenomatous polyposis coli (APC) protein as a candidate
87 Trabid substrate (Tran et al. 2008). Trabid knockdown in HEK293 cells caused APC to become
88 modified with polyubiquitin and aggregate in the cytoplasm, whereas high Trabid levels
89 correlated with *hypo*ubiquitylated APC that accumulated in the membrane protrusions of long
90 cell processes. These observations led us to propose that Trabid regulates the ubiquitylation and
91 subcellular localisation of APC (Tran et al. 2013). In neurons, APC organises the cortical
92 cytoskeleton to promote the formation of growth cones and the steering of growing axons that
93 are essential for embryonic brain development (Yokota et al. 2009; Preitner et al. 2014;

94 Dogterom and Koenderink 2019; Efimova et al. 2020). High expression of Trabid, APC and
95 STRIPAK proteins in neural stem cells (Castets et al. 2000; Blanpain et al. 2004; Yokota et al.
96 2009) indicate that Trabid's association with STRIPAK and its ability to regulate APC
97 polyubiquitylation may be important for neurogenesis. We now show that two Trabid mutants
98 found in children with developmental deficits are impaired in two distinct biochemical activities
99 that culminate in the perturbed trafficking of APC to neurite tips. We propose that the neuronal
100 and developmental phenotypes associated with these Trabid loss-of-function mutations are
101 primarily caused by the mislocalisation of APC that leads to defective cytoskeleton organisation
102 and aberrant cell locomotion.
103
104
105 **Results**
106 **Trabid patient variants are impaired in DUB activity and STRIPAK binding**
107 *Trabid/ZRANB1* patient missense mutations, R438W and A451V, are linked to developmental
108 microcephaly (Deciphering Developmental Disorders 2015). Mapping these residues onto the
109 domain structure of Trabid show that they flank either side of Trabid's catalytic cysteine C443
110 (Fig. 1A). Residue R438 projects prominently into the catalytic cleft formed by the ankyrin
111 repeats and the OTU core of Trabid's catalytic domain (Licchesi et al. 2012), whereas residue
112 A451 resides at the back of the active site, opposite to C443 on alpha helix 4 (Fig. 1B). To
113 determine if patient mutations R438W and A451V influence substrate catalysis, we purified the
114 mutant AnkOTU domains and tested their ability to hydrolyse synthetic ubiquitin chains *in vitro*
115 (Licchesi et al. 2012). Wild-type Trabid AnkOTU generated appreciable amounts of mono-
116 ubiquitin within 15 min incubation with either Lys29- or Lys63-linked di-ubiquitin chains (Fig
117 1C and D). In contrast, Trabid R438W showed near total loss of DUB activity and cleaved
118 ubiquitin product was only readily detected after a prolonged 120 min incubation (Fig. 1C and
119 D). A catalytically inactive C443S mutant AnkOTU domain failed to hydrolyse ubiquitin chains
120 even after 2 h incubation (Fig. 1C and D). Interestingly, the Trabid A451V AnkOTU domain
121 cleaved Lys29- or Lys63-linked di-ubiquitin with comparable efficiency to wild type Trabid,
122 despite it being slightly less stable as a recombinant protein based on thermal stability assay
123 (Supplementary Fig. 1A). A ubiquitin suicide probe assay revealed that R438W and A451V

124 Trabid AnkOTU proteins retained a functional catalytic interaction with ubiquitin
125 (Supplementary Fig. 1B).
126
127 In cells, the inability of the DUB-inactive Trabid C443S to cleave polyubiquitin led to stable
128 interaction of this mutant with polyubiquitylated substrates (Tran et al. 2008; Licchesi et al.
129 2012). We therefore asked whether the DUB-impaired R438W Trabid likewise exhibited
130 increased binding to polyubiquitin in cells. Polyubiquitin chains readily co-precipitated with both
131 FLAG-tagged Trabid R438W and FLAG-Trabid C443S expressed in HEK293T cells, consistent
132 with the compromised DUB activity of these mutants (Fig. 1E). The Trabid A451V variant did
133 not co-precipitate abundant polyubiquitylated substrates, consistent with it retaining full DUB
134 activity (Fig 1E).
135
136 We have previously identified an interaction between Trabid and STRIPAK that is important for
137 the deubiquitylation of substrate APC (Tran et al. 2013). Whilst A451V retained full DUB
138 activity, strikingly, in contrast to FLAG-Trabid wild-type, R438W and C443S, the FLAG-Trabid
139 A451V mutant failed to efficiently co-precipitate several STRIPAK components, including
140 Striatin3 and STRIP1 (Fig. 1E). All FLAG-Trabid proteins co-precipitated similar levels of the
141 substrate E3 ubiquitin ligase HECTD1 (Tran et al. 2013; Harris et al. 2021). Together, these
142 results suggest that the Trabid patient mutations produce hypomorphic variants impaired in two
143 distinct biochemical activities: polyubiquitin hydrolysis and STRIPAK-binding.
144
145 **Decreased cell density in the brains of mice harbouring Trabid patient mutations**
146 Given the microcephaly observed in children with Trabid mutations, and to understand the
147 consequence of Trabid hypomorphic variants *in vivo*, we examined knock-in mice carrying
148 Trabid patient mutations for evidence of brain development abnormalities (Fig. 2A). Mice
149 heterozygous or homozygous for the R438W or A451V mutation were viable, fertile, and born at
150 expected Mendelian ratios (Fig. 2B). Given that germline Trabid knockout or C443S
151 homozygous knock-in mice exhibit perinatal lethality (Dickinson et al. 2016) (our unpublished
152 data), these new R438W and A451V mutant mouse strains allow us to interrogate Trabid
153 function *in vivo*. Homozygous mutant mice from the R438W colony weighed on average ~15%
154 less than wild-type littermates, while R438W hemizygous and A451V mutant mice did not

155 exhibit significant weight loss (Fig. 2C). Immunohistochemical analysis of brain sections from
156 weaned littermate mice of both mutant strains revealed normal structure and laminar organisation
157 of the cerebral cortex, but intriguingly a reduction in cell number was apparent in different brain
158 regions of R438W and A451V homozygous mice compared to similar wild-type littermate
159 controls (Fig. 2D). Ctip2+ neurons in the striatum of R438W and A451V mutant mice were also
160 reduced compared with wild-type littermates (Fig. 2E). Homozygous mice showed a greater cell
161 number loss than hemizygous mice, suggesting a gene dosage effect. Moreover, R438W and
162 A451V mutant mice had reduced number of Olig2+ oligodendrocytes in the forebrain and
163 midbrain compared to wild-type littermate mice (Fig. 2F). Olig2+ oligodendrocytes in
164 homozygous brain sections were consistently strongly reduced (>30%) compared to wild-type
165 mice, independent of age or sex. Of a combined 16 sets of littermate mice from both R438W and
166 A451V colonies, reduced neuronal or glial cell numbers were conspicuous in homozygous brain
167 sections of 12 littermate sets (Fig. 2E, F; see also Fig. 3), indicating incomplete penetrance of the
168 mutant phenotype. Collectively, these results suggest that Trabid's DUB and STRIPAK-binding
169 activities are required to produce the correct numbers of neuronal and glial cells in the
170 developing brain.
171
172 **Trabid mutant mice exhibit a motor deficit consistent with reduced numbers of**
173 **dopaminergic neurons and projections**
174 Given the cell number deficits in the midbrain of Trabid mutant mice and the reported midbrain
175 neurodegeneration and locomotor defects in Trabid mutant *Drosophila* (Kounatidis et al. 2017),
176 we asked if the numbers of dopaminergic neurons that control motor function might be affected
177 in Trabid R438W and A451V mutant mice. Midbrain and striatal coronal sections were
178 immunostained for Tyrosine Hydroxylase (TH), the rate-limiting enzyme for dopamine synthesis
179 and a marker of dopaminergic neurons. A reduction in the numbers of TH+ neurons was
180 observed in the substantia nigra pars compacta (SNc) of Trabid mutant mice from both R438W
181 and A451V colonies, independent of age or sex (Fig. 3A). SNc neurons project axons to the
182 striatum to produce an extensive network of axonal terminals that communicate with striatal
183 neurons (Matsuda et al. 2009). Consistent with the lack of prominent TH+ neuronal processes
184 emanating from the SNc neurons that remain in the mutant midbrain, TH immunoreactivity was
185 reduced in the striatum of homozygous R438W and A451V mutant mice (Fig. 3B, C). Also in

186 mutant brain sections, the reduced abundance and intensity of TH+ neuronal processes were
187 readily apparent in cortical regions including the motor cortex and claustrum that regulate motor
188 responses (Fig. 3B, C). Differences in TH staining in the mutant striatum compared to wild type
189 were modest or not observed in all littermates examined (Fig. 3D), indicating incomplete
190 penetrance of the mutant Trabid alleles.
191
192 Given the altered abundance of TH+ cells and projections in motor-related brain regions of
193 Trabid mutant mice, we evaluated the motor function of these mice using a rotarod assay.
194 Homozygous R438W mice showed a significantly reduced latency to fall at 20, 25, 30 and 35
195 RPM, compared to controls (Fig. 3E), as did homozygous A451V animals at 30 and 35 RPM
196 (Fig. 3E). This indicates that Trabid patient mutations impair motor coordination, consistent with
197 a deficiency in dopaminergic neurons. The smaller size of R438W homozygous mice compared
198 to wild-type littermates (Fig. 2C) could be a contributing factor to the compromised rotarod
199 performance of these mutants. However, given that A451V homozygous mice on average are not
200 smaller than wild-type littermates, the motor deficit exhibited by both R438W and A451V
201 homozygous mice is likely caused by the abnormal cell numbers and reduced dopaminergic
202 neurons in their brains (Figs. 2 and 3). Taken together, these results suggest that Trabid regulates
203 the brain cellular architecture and circuitry required for normal motor function.
204
205 **Trabid patient mutants fail to efficiently limit APC ubiquitylation in cells**
206 To understand the molecular basis for the neuronal and behavioral phenotypes of Trabid mutant
207 mice, we focused on APC— an established regulator of mammalian brain development (Yokota
208 et al. 2009; Preitner et al. 2014) and a protein that we have shown becomes strongly
209 ubiquitylated upon loss of Trabid or Striatin (Tran et al. 2008; Tran et al. 2013). Moreover, given
210 that Striatin binds directly to APC (Breitman et al. 2008), we hypothesized that the Trabid
211 patient mutants impaired in DUB activity or Striatin-binding would impact APC ubiquitylation
212 and function in cells. To test this, we generated cells with doxycycline (dox)-inducible
213 expression of FLAG-Trabid and examined the ubiquitylation status of endogenous APC in dox-
214 treated cells. The levels of ubiquitin-modified APC were strongly suppressed in cells expressing
215 wild-type FLAG-Trabid (Fig. 4). In contrast, induction of the FLAG-Trabid R438W mutant, like
216 the catalytically dead FLAG-Trabid C443S, did not repress APC ubiquitylation, and induction of

217 FLAG-Trabid A451V expression only partially reduced APC ubiquitylation compared to control
218 cells (Fig. 4). These results suggest that both DUB and STRIPAK-binding activities of Trabid
219 are required for efficient deubiquitylation of APC in cells.
220
221 **Trabid patient mutants impede EGFP-APC transport to the leading edge of migrating cells**
222 APC decorates the membrane protrusions at the leading edge of migrating cells (Nathke et al.
223 1996) and we have shown that Trabid is a key regulator of APC localisation to these cortical
224 structures (Tran et al. 2013). Consistent with this insight, FLAG-Trabid localised prominently
225 with EGFP-APC in the tips of long cell processes (Fig. 5A). Analysis of several of these tip
226 clusters by super resolution microscopy revealed ~30% overlap between the FLAG-Trabid and
227 EGFP-APC signals, indicating that a significant fraction of these proteins co-localise in cortical
228 cell protrusions (Fig. 5B). In sub-confluent cultures, EGFP-APC localised strongly to the
229 lamellipodial leading-edge of the majority of cells co-transfected wild-type FLAG-Trabid (Fig.
230 5C, D). By contrast, in cells transfected with the FLAG-Trabid mutants R438W and A451V,
231 EGFP-APC formed irregular puncta at sub-cortical regions close to the leading edge and EGFP-
232 APC aggregates are often sequestered to puncta formed by the R438W FLAG-Trabid mutant
233 (Fig. 5C, D). Such sites may contain ubiquitylated substrates bound to DUB-defective Trabid
234 mutants, as we have previously demonstrated with Trabid C443S (Tran et al. 2008; Licchesi et
235 al. 2012). Consistently, FLAG-Trabid C443S formed puncta that contained EGFP-APC near the
236 tips of long cell processes (Fig. 5E). Intriguingly, the Trabid substrate HECTD1 was sequestered
237 to C443S puncta in the cytosol, but not to puncta residing near the leading-edge membrane (Fig.
238 5E). In confluent cultures following prolonged co-transfection of FLAG-Trabid mutants and
239 EGFP-APC, we observed the striking phenomena of strong EGFP-APC aggregation on or near
240 the plasma membrane and nanotube-like processes extending between neighbouring cells
241 decorated with abundant EGFP-APC puncta/aggregates of various sizes (Fig. 5F). Collectively,
242 these results indicate that Trabid's DUB and STRIPAK-binding activities are required for the
243 efficient localisation of APC to plasma membrane sites involved in polarised cell migration.
244
245 **Trabid patient mutations perturb the axonal trafficking of APC-tdTomato and impair the**
246 **trajectory of neurite outgrowth**

247 APC regulates the dynamic interactions of the microtubule and actin cytoskeletons at cortical
248 membranes to direct the formation of neuronal growth cones and the trajectory of axon growth
249 (Dogterom and Koenderink 2019). To investigate the effect of patient Trabid mutations on APC
250 localisation in primary neurons, we generated mice expressing an APC-tdTomato fluorescent
251 protein under the control of the endogenous *Apc* gene promoter (Fig. 6A). APC-tdTomato mice
252 were bred with knock-in mice carrying either the Trabid R438W or A451V mutant allele (Fig. 2)
253 and neural progenitors were isolated at embryonic day E11.5 from compound heterozygotes. We
254 then performed live cell imaging to analyse the trafficking of APC-tdTomato in neurites
255 extending from progenitors undergoing differentiation (Fig. 6A). Endogenous Trabid protein
256 levels were comparable in neural progenitor cultures derived from embryos bearing wild-type or
257 R438W and A451V mutant Trabid alleles (Fig. 6B). In neurons with wild-type Trabid, APC-
258 tdTomato accumulated strongly in the tips of growing neurites, marking prominent growth cones
259 that drive axon elongation (Fig. 6C; *Zranb1*$^{+/+}$). In neurons with hemizygous Trabid R438W or
260 A451V mutation, APC-tdTomato exhibited broad distribution along the length of the neurite and
261 the formation of growth cones were severely compromised (Fig. 6C, *Zranb1*$^{R438W/+}$). Tracking
262 analysis of the turn angles of APC-tdTomato intensities revealed that neurites with wild-type
263 Trabid elongated in a polarised manner, whereas neurites with R438W or A451V mutant Trabid
264 turned back or retracted at a greater frequency (Fig. 6D and E). These data suggest that Trabid's
265 DUB and STRIPAK-binding activities are required for efficient transport of APC to neurite tips
266 to promote the formation growth cones required for polarised axon elongation.
267
268
269 **Discussion**
270 We describe a novel function for the deubiquitylating enzyme Trabid as a key regulator of
271 axonal growth and guidance that likely underpins the neurodevelopmental defects observed in
272 children with Trabid mutation. Our data suggests that Trabid's mechanism of action is to
273 suppress the ubiquitylation of APC to regulate its intracellular trafficking. A *hypo*ubiquitylated
274 APC pool is efficiently localised to the cortical cytoskeleton where it directs neuronal growth
275 cone formation and polarised axon elongation. The identification of human Trabid variants that
276 disrupt the distribution of APC to the leading edge of migrating cells provides a plausible
277 explanation for the associated patient neuro-developmental disorders. Our work identifies

278 Trabid's DUB- and STRIPAK-binding activities, and the control of APC localisation, as crucial
279 events during embryonic and neural development.
280
281 The two patients carrying Trabid missense mutations R438W and A451V were diagnosed with a
282 range of distinct congenital disorders including craniofacial abnormalities, seizures,
283 developmental delay, autism—and both patients presented with microcephaly and constipation
284 (Deciphering Developmental Disorders 2015). We propose that the underlying cause of these
285 seemingly unrelated conditions, broadly classified as neurocristopathies, is the abnormal
286 specification or migration of neural crest cells in the developing embryo (Vega-Lopez et al.
287 2018). Discrete neural crest populations contribute to the development of craniofacial structures,
288 the forebrain and midbrain, and the enteric nervous system (Anderson et al. 2006; Creuzet et al.
289 2006). Therefore, errors in the formation or polarised migration of neural crest cells could
290 account for all the patient phenotypes, including the reduction in brain volume (microcephaly).
291 Presently, we can only speculate that the irregular cellular architecture and reduced cell numbers
292 in the brains of mice harbouring Trabid patient mutations (Figs. 2 and 3) reflect the errant
293 migration of neural crest or neural progenitor cell populations in early embryogenesis (Silva et
294 al. 2019). While Trabid mutant mice did not exhibit microcephaly, they showed a motor deficit
295 (Fig. 3) consistent with the locomotor defects reported for Trabid loss-of-function in *Drosophila*
296 (Kounatidis et al. 2017). Intriguingly, the fly Striatin homolog CKA is involved in axonal
297 transport and motor coordination (Neisch et al. 2017), and *Drosophila* Strip1 regulates
298 endosomal trafficking and axon elongation (Sakuma et al. 2014). Endosomal trafficking defects
299 have been linked to reduced proliferation of neural progenitors and microcephaly (Carpentieri et
300 al. 2022). Three independent groups have identified Trabid's association with STRIPAK (Sowa
301 et al. 2009; Tran et al. 2013; Harris et al. 2021). We have now established the functional
302 significance of this interaction. The requirement of Trabid binding to STRIPAK for efficient
303 protein trafficking, polarised axon growth, and motor coordination (Figs. 3, 5, 6), supports the
304 view that Trabid-STRIPAK regulates an evolutionarily conserved mechanism of cell movement
305 required for normal brain development and establishment of the correct neuronal circuitry in the
306 motor system.
307

308 The impairment of two distinct Trabid functions—polyubiquitin hydrolysis and STRIPAK-
309 binding—led to common cellular, developmental, and behavioral phenotypes (Figs. 2-6)
310 (Deciphering Developmental Disorders 2015), strongly suggesting that these activities act in the
311 same pathway. We propose that APC is the primary molecular target of Trabid action in
312 cytoskeleton organisation and polarised axon growth (Fig. 7). APC is an established regulator of
313 cell adhesion and migration, and it governs the cortical actin and microtubule cytoskeleton
314 dynamics required to form and steer axonal growth cones (Dogterom and Koenderink 2019;
315 Efimova et al. 2020). In a yeast two hybrid screen, we have found that Trabid and Striatin
316 interacted with the armadillo repeat domain (ARD) of APC, but not to an APC ARD mutant that
317 caused cell-cell adhesion defects (Hamada and Bienz 2002; Tran et al. 2008). This implies that a
318 functional interaction between Trabid, Striatin and APC promotes the fidelity of cell-cell or cell-
319 substratum contacts. Our model of Trabid action in Figure 7 integrates published data showing
320 that (1) Trabid complexes with Striatin/STRIPAK in human cell lines (Sowa et al. 2009; Tran et
321 al. 2013; Harris et al. 2021), and (2) Striatin binds directly to the ARD domain of APC (Breitman
322 et al. 2008). We propose that STRIPAK recruits Trabid to deubiquitylate APC. This allows APC
323 to accumulate at the leading edge of migrating cells to promote efficient, polarised locomotion
324 (Fig. 7A). The Trabid R438W mutant still binds STRIPAK and is recruited to APC, but it is
325 impaired in its ability to cleave ubiquitin chains from APC. And although the Trabid A451V
326 mutant retains full DUB activity, it cannot be recruited to APC via STRIPAK. Both mutant
327 scenarios cause APC to become persistently modified with ubiquitin chains that lead to APC
328 delocalisation from cell tips and defective cell movement (Fig. 7B). Consistent with this model,
329 Trabid or Striatin deficiency caused APC hyperubiquitylation and aggregation, perturbed actin
330 assembly and microtubule stability, and inhibited the migration of mouse and human cell lines
331 (Bai et al. 2011; Tran et al. 2013) (our unpublished data). Optimal cell adhesion and migration
332 requires stable, acetylated microtubules (Aguilar et al. 2014; Bance et al. 2019). Of note, loss of
333 APC and the STRIPAK proteins STRIP1 and CTTNBP2 strongly reduced the acetylated
334 microtubule network in neurons (Yokota et al. 2009; Shih et al. 2014; Sakuma et al. 2015).
335 Furthermore, Striatin depletion perturbed cell-cell adhesion (Breitman et al. 2008; Lahav-Ariel et
336 al. 2019) and axon elongation defects caused by STRIP1 mutation are linked to the dysregulation
337 of neuronal adhesion (Sakuma et al. 2014). It would be interesting to investigate if chronic APC
338 ubiquitylation and dysfunction underlie all Trabid and STRIPAK mutant phenotypes.

339 **Materials and Methods**

340 **Protein purification and characterisation**

341 Wild type (WT), R438W, A451V, and C443S Trabid AnkOTU domains (245-697) were
342 expressed in BL21 competent *E. coli* and purified as described previously (Licchesi et al. 2012)
343 with minor modifications. *E. coli* cells were induced with 300 mM IPTG and grown overnight at
344 16 °C. Cells were lysed by sonication in 50 mL lysis buffer (20 mM Tris pH 8.5, 200 mM NaCl,
345 10% glycerol, 1 mM PMSF, 2x Roche protease inhibitor tablets, 3 mM $MgCl_2$, 0.1 mg/mL
346 DNAse, 150 µL lysozyme, 10 mM β-mercaptoethanol) per 2 L culture. Anion-exchange
347 chromatography (MonoQ 5/50) was performed using the ÄKTA pure system at 4 °C. See
348 Supplementary Fig. S1 for the characterisation of the thermal stability and ubiquitin reactivity of
349 purified Trabid AnkOTU proteins. For DUB assays, a total of 20 µL reaction consisting of 0.25
350 µM purified AnkOTU domain was incubated with 1 µM of K29, K63 di-ubiquitin chains, or
351 K33-linked Tetra-Ub chains (R&D Systems) in DUB reaction buffer (50 mM NaCl, 50 mM Tris
352 pH 7.4, and 5 mM DTT) at 37 °C. Reactions were stopped at the indicated times by addition of
353 SDS sample buffer and visualized by SDS-PAGE and silver staining (Silver Stain Plus; Biorad).
354

355 **Plasmid transfection, cells, and antibodies**

356 An inducible lentiviral CRISPR/Cas9 system (Aubrey et al. 2015) was used to overexpress
357 Trabid in Figure 4. PCR amplified DNA encoding human wild-type or mutant Trabid with an N-
358 terminal FLAG tag was cloned into the EcoRI/NheI sites of a doxycycline-inducible pFTREtight
359 MCS rtTAadvanced puro lentiviral vector (Brumatti et al. 2013). Transduced HEK293 cells were
360 selected for puromycin resistance and pooled clones were used for experiments. Transient
361 transfection of plasmids pcDNA3.1-FLAG-Trabid (Tran et al. 2013), FLAG-Trabid mutants
362 generated by site-directed mutagenesis, pEGFP-C1-APC (Rosin-Arbesfeld et al. 2001), and
363 pCMV-HA-HECTD1 (Sarkar and Zohn 2012) in HEK293T cells was performed using
364 Lipofectamine 2000 (Invitrogen). HEK293/T cells were cultured in DMEM supplemented with
365 10% FBS and 2 mM L-Glutamine in a humidified incubator at 37ºC with 5% CO_2. Mouse
366 monoclonal Trabid antibodies and rabbit polyclonal HectD1 antibodies have been described
367 (Tran et al. 2008; Tran et al. 2013). Commercial antibodies were purchased from a variety of
368 vendors: anti-APC ALi 12-28 (Santa Cruz), anti-Striatin (BD Biosciences), anti-Striatin3
369 (SG2NA, Novus Biologicals), anti-Strip1 (Abcepta) anti-ubiquitin P4D1 (Cell Signaling), anti-

370 FLAG M2, anti-β-actin-HRP AC-15, anti-β-tubulin (Sigma), anti-HA 3F10 (Roche), anti-
371 Tyrosine Hydroxylase (Millipore, AB152), anti-Ctip2 (Abcam, ab18465), and anti-Olig2
372 (Abcam, ab109186).
373
374 **Protein enrichment from cell lysates**
375 Confluent cells in 10 cm dishes were lysed on ice in 1 mL lysis buffer containing 1% IGEPAL
376 CA-630, 50 mM Tris-HCl, pH 7.5, 120 mM NaCl, 1 mM EDTA, and protease inhibitor tablets
377 (Roche). Lysates were centrifuged at 14,000 rpm for 10 min to remove cell debris. The
378 supernatant was assayed for protein (BCA kit, Pierce), then 1 mg total protein was
379 immunoprecipitated with anti-FLAG M2 antibody and protein G sepharose in a total volume of 1
380 mL lysis buffer. Enrichment of polyubiquitin chains was performed using purified GST-TUBE
381 (Tandem Ubiquitin Binding Entity) protein (Hjerpe et al. 2009). A volume of cell supernatant
382 containing 1 mg total protein was diluted 1:1 with 4M urea then incubated with 10 μg GST-
383 TUBE and Glutathione sepharose 4B. Immunoprecipitations and GST-TUBE pulldowns were
384 performed overnight with constant rotation at 4°C. Protein complexes were washed twice with
385 lysis buffer and once with PBS, then eluted at 95°C for 5 min in Laemmli buffer for Western
386 blotting analysis.
387
388 **Mice**
389 All mouse studies complied with relevant ethical regulations and were approved by the Walter
390 and Eliza Hall Institute Animal Ethics Committee. The *Zranb1*^{R438W}, *Zranb1*^{A451V}, and *Apc*^{tdTomato}
391 knock-in mice were generated on a C57BL/6J background using CRISPR–Cas9-mediated gene
392 editing by the Melbourne Advanced Genome Editing Centre (MAGEC) at the Walter and Eliza
393 Hall Institute. To generate a R438W mutation within the *Zranb1* gene on mouse chromosome 7,
394 a single guide (sg) RNA of the sequence GAC TAT ATG CAC TTT GGA AC was used to
395 create double stranded breaks within the Zranb1 locus to stimulate homologous recombination
396 and an oligo donor of the sequence TAT AAA CTG GTC TTT GGA GTT GGC TAC ACG TCT
397 GGA CAG TAG ACT ATA TGC ACT TTG GAA CTG GAC TGC CGG AGA TTG TTT ACT
398 TGA CTC AGT ACT ACA AGC TAC ATG GGG CAT TTA TGA CAA A was used to
399 introduce the R438W mutation. The sgRNA and donor sequence along with Cas9 mRNA were
400 injected into the cytoplasm of fertilized one-cell stage embryos generated from wild-type

401 C57BL/6J breeders. To generate the A451V mutation, a sgRNA of the sequence ACT CAG TAC
402 TAC AAG CTA CA and an oligo donor of the sequence ACA GTA GAC TAT ATG CAC TTT
403 GGA ACC GGA CTG CCG GAG ATT GTT TAC TTG ACT CAG TAC TAC AAG TCA CAT
404 GGG GCA TTT ATG ACA AAG ACT CGG TGC TTC GGA AAG CCC TGC ATG ACA GCC
405 TG CAT was used. Twenty-four hours later, two-cell stage embryos were transferred into the
406 uteri of pseudo-pregnant female mice. Viable offspring were genotyped by next-generation
407 sequencing. Targeted animals were backcrossed twice to wild-type C57BL/6J to eliminate off-
408 target mutations. Generation of C57BL/6J mice expressing the APC-tdTomato fusion protein
409 under the control of the endogenous *Apc* promoter (B6J.*Apc*^{tdTom}) were based on methods
410 previously described (Ng et al. 2020). Briefly, a sgRNA of the sequence AGA CGT CAC GAG
411 GTA AGA CC was used to create double stranded breaks within the *Apc* locus to stimulate
412 homologous recombination. A targeting vector containing homology arms of ~1.4 kilobases was
413 used to introduce the tdTomato coding sequence after the last *Apc* coding exon. Forward (ACC
414 TGT TCC TGT ACG GCA TG) and reverse (GCC TCC CAA AAT GAC CAG TG) primers to
415 detect the tdTomato sequence were used to screen viable pups for integration of the targeting
416 vector by PCR.
417
418 **Neurite outgrowth from cultured neural progenitors**
419 To generate mouse embryos expressing Apc-tdTomato with wild-type or mutant Trabid, mice
420 heterozygous for the Apc-tdTomato allele (*Apc*$^{tdTom/+}$) were outcrossed with mice heterozygous
421 for the Trabid R438W or A451V mutant allele (*Zranb1*$^{R438W/+}$ or *Zranb1*$^{A451V/+}$). Embryos at
422 E11.5 were harvested from pregnant females and ventral midbrains were dissected as previously
423 described (Thompson and Parish 2013). The isolated midbrain tissue was enzymatically
424 dissociated in Hank's Balanced Salt Solution containing 0.05% trypsin and 0.1% DNase I for 12
425 minutes at 37°C. Cells in the tissue were separated by mechanical dissociation, counted, then
426 plated in serum-free N2 medium consisting of a 1:1 mixture of Ham's F12 and Minimum
427 Essential Medium supplemented with 15 mM HEPES buffer, 1 mM glutamine, 6 mg/ml glucose,
428 1 mg/ml bovine serum albumin and N2 100X supplement. Cells were seeded at a density of
429 250,000 cells per well in a 24-well plate at 37°C, 3% CO_2. An aliquot of the resultant
430 neurosphere cultures were sequenced to ascertain genotypes. To differentiate midbrain
431 progenitors towards the dopaminergic lineage, neurospheres were resuspended in N2 medium

432 containing BDNF and GDNF (30 ng/ml each) then seeded in tissue culture dishes or glass
433 bottom ibidi chamber slides pre-coated with poly-D-lysine and laminin (10 μg/ml each).
434
435 **Histology and IHC analysis**
436 Mice were euthanized by CO_2 inhalation and intracardial perfusion was performed to fix the
437 tissues. Perfusion was initiated with Dulbecco's phosphate buffered saline followed by 10%
438 neutral buffered formalin (NBF). After perfusion, brain and tissues were dissected and post-fixed
439 in 10% NBF for 24h before paraffin-embedding with the Tissue-Tek VIP 6 automated tissue
440 processor (Sakura Finetek USA). Formalin-fixed paraffin-embedded tissues were sectioned
441 into 7 μm slices using a microtome and mounted on positively charged slides.
442 Immunohistochemistry (IHC) was performed with the Omnis Auto-immunostaining platform
443 using Agilent EnVision Target retrieval solution and the optimal dilution of the primary antibody
444 against the target protein. Secondary antibody detection was performed with the
445 Dako EnVision+ Single Reagents HRP and FLEX DAB+ Substrate Chromogen System. Slides
446 were counterstained with haematoxylin. Sections from wild-type, heterozygous and homozygous
447 littermate mice were mounted and stained on the same slide to ensure IHC signals can be directly
448 compared. Cell counts and IHC signal intensities were quantified using Fiji software (NIH). The
449 workflow for counting cells from IHC images is described in Supplementary Figure 2. IHC
450 signal intensities were measured as the optical density proportional to the concentration of the
451 stain. Briefly, the colour spectra of DAB- and haematoxylin-stained image was separated by
452 colour deconvolution, converted to greyscale, thresholding was applied, and the mean pixel
453 intensity of the region of interest was measured.
454
455 **Rotarod performance test**
456 The motor coordination of 3- to 4-month-old littermate mice from Trabid R438W and A451V
457 colonies were measured using a rotating rod (Rotamex-5, Columbus Instruments). Mice were
458 lowered onto a 3 cm diameter rod rotating at 12, 16, 20, 25, 30, 35, 40 or 45 revolutions per min
459 (RPM) for 2 min or until they fell. Animals were given a 5 min rest between RPM sessions. Two
460 trials were performed with a 1 h break between trials. The latency to fall was recorded for each
461 RPM. A 1 sec penalty was added if an animal failed to walk in time with the rod but rather
462 gripped the rod and rotated with it (cartwheel). Animals underwent 2 trials per day across 3 days.

463

464 **Microscopy and image analysis**

465 *Confocal microscopy* – Cells grown in MatTek chamber slides were fixed with 4%
466 paraformaldehyde for 10 min at room temperature, then permeabilized with 0.2% Triton-X100
467 and blocked with 5% normal goat serum (NGS). Cells were incubated with primary antibodies
468 diluted in 5% NGS overnight at 4ºC, followed by Alexa Fluor-conjugated secondary antibodies
469 for 1h at room temperature. ProLong Gold antifade reagent with DAPI was used to mount
470 coverslips to microscope slides. Confocal images were acquired on a Zeiss LSM 880 Airyscan
471 microscope using a 63x/1.4 N.A. oil objective, and 405, 488 and 594nm lasers. Maximum
472 intensity projections of raw images comprising 10-15 *z* sections were created using Fiji.

473

474 *3D structured illumination microscopy* – Super-resolution three-dimensional structured
475 illumination microscopy (3D-SIM) was performed on the DeltaVision OMX-SR system using
476 a 60x/1.42 N.A. PlanApo oil immersion objective, sCMOS cameras, and 488, 568 and 640 nm
477 lasers. 3D-SIM images consisted of 15 raw images per focal plane per colour channel with 125
478 nm between each z-step. Images were reconstructed and the colour channels aligned using the
479 reconstruction and alignment algorithms in softWoRx 7.0. Fraction of overlap between FLAG-
480 Trabid and EGFP-APC were measured in Imaris 9.2.

481

482 *Lattice lightsheet time-lapse imaging and analysis* – Live cell time-lapse imaging of APC-
483 tdTomato fluorescence in growing neurites was acquired using the Zeiss Lattice Light Sheet 7
484 microscope. A 561 nm laser formed a light sheet of length 30 µm with a thickness of 1 µm at the
485 sample plane via a 13.3 x, 0.44 NA objective. tdTomato fluorescence was collected via a 44.83
486 X, 1 NA detection objective lens. Data was collected with a frame rate of 60 ms and a z-step of
487 300 nm. Each region was imaged at 15-min intervals for 4-6 hours. Fluorescence was collected
488 via a multi-band stop, LBF 405/488/561/633, filter. Images were subsequently deskewed using
489 Zeiss's Zen 3.4 software. Samples were measured at 37 °C and 5% CO_2. Maximum intensity
490 projections were created from the deskewed data in Fiji. Neurite tips were tracked using
491 Trackmate (v6.0.3) and LoG detector with 12 µm diameter, 0.08 threshold, no filters, and
492 subpixel localisation turned on. A minimum of 5 frames were set for track inclusion. Turn angles
493 were calculated using Matlab R2019b. Three points were used to calculate the turn. The first two

points determine the direction of neurite growth. The angle between this direction to the third point determines the turn angle of the neurite. The turn angle was normalized such that 0º constitutes a step straight forward with no turn and 180º is a turn backwards.

Acknowledgements

We thank Prof David L. Vaux for his generous support and mentorship in the early stages of this study. We thank Drs S. Wilcox, S. Scutts, D. Newgreen, J. Vince, C. Parish, M. Herold, T. Thomas, K. Newton and V. Dixit for discussion, reagents and technical support; and WEHI's Bioservices staff for outstanding animal care. Part of the funding for this study was provided by the Australian National Health and Medical Research Council (Ideas Grant #1181580 to E.V., H.T., and B.M.T). G.D. was supported by a fellowship from the Bodhi Education Fund. Work in the authors' laboratory is made possible by operational infrastructure grants through the Australian Government Independent Research Institutes Infrastructure Support (IRISS) and the Victorian State Government OIS. The generation of all mutant and transgenic mice used in this study was supported by Phenomics Australia and the Australian Government through the National Collaborative Research Infrastructure Strategy (NCRIS) program.

Author Contributions

D.F. designed and performed the protein biochemistry experiments, quantified cell numbers from histological sections, and assisted with the generation and maintenance of neurosphere cultures. M.B. designed and performed the rotarod experiments and assisted with analysis of the rotarod and histology data. M.M. performed 3D-SIM microscopy, live cell imaging of Apc-tdTomato, and analysed the data. A.K. designed the targeting vectors for generation of knock-in mice. E.T. assisted with the design of histology experiments. C.H. performed the genotyping. G.K. assisted with statistical analysis of the rotarod data and quantified IHC intensities. A.V., C.M., M.F., K.R., B.T., and E.V. analysed data. D.K. analysed data and provided study feedback and advice. G.D. supervised the study, analysed and conceptualized data, and edited the manuscript. H.T. conceived the project, designed, performed and supervised experiments, analysed and conceptualized data, and wrote the manuscript. All authors have read and commented on the manuscript.

525

526

527 **Competing Interest Statement**

528 D.K. is founder, shareholder and serves on the SAB of Entact Bio.

529

530

531 **References**

532 Aguilar A, Becker L, Tedeschi T, Heller S, Iomini C, Nachury MV. 2014. Alpha-tubulin K40
533 acetylation is required for contact inhibition of proliferation and cell-substrate adhesion.
534 *Mol Biol Cell* **25**: 1854-1866.

535 Anderson RB, Newgreen DF, Young HM. 2006. Neural crest and the development of the enteric
536 nervous system. *Adv Exp Med Biol* **589**: 181-196.

537 Aubrey BJ, Kelly GL, Kueh AJ, Brennan MS, O'Connor L, Milla L, Wilcox S, Tai L, Strasser A,
538 Herold MJ. 2015. An inducible lentiviral guide RNA platform enables the identification of
539 tumor-essential genes and tumor-promoting mutations in vivo. *Cell Rep* **10**: 1422-1432.

540 Bai SW, Herrera-Abreu MT, Rohn JL, Racine V, Tajadura V, Suryavanshi N, Bechtel S, Wiemann
541 S, Baum B, Ridley AJ. 2011. Identification and characterization of a set of conserved and
542 new regulators of cytoskeletal organization, cell morphology and migration. *BMC Biol* **9**:
543 54.

544 Bance B, Seetharaman S, Leduc C, Boeda B, Etienne-Manneville S. 2019. Microtubule acetylation
545 but not detyrosination promotes focal adhesion dynamics and astrocyte migration. *J Cell*
546 *Sci* **132**.

547 Bazzi H, Soroka E, Alcorn HL, Anderson KV. 2017. STRIP1, a core component of STRIPAK
548 complexes, is essential for normal mesoderm migration in the mouse embryo. *Proc Natl*
549 *Acad Sci U S A* **114**: E10928-E10936.

550 Beck DB, Basar MA, Asmar AJ, Thompson JJ, Oda H, Uehara DT, Saida K, Pajusalu S, Talvik I,
551 D'Souza P et al. 2021. Linkage-specific deubiquitylation by OTUD5 defines an embryonic
552 pathway intolerant to genomic variation. *Sci Adv* **7**.

553 Blanpain C, Lowry WE, Geoghegan A, Polak L, Fuchs E. 2004. Self-renewal, multipotency, and
554 the existence of two cell populations within an epithelial stem cell niche. *Cell* **118**: 635-
555 648.

556 Breitman M, Zilberberg A, Caspi M, Rosin-Arbesfeld R. 2008. The armadillo repeat domain of
557 the APC tumor suppressor protein interacts with Striatin family members. *Biochim Biophys*
558 *Acta* **1783**: 1792-1802.
559 Brumatti G, Salmanidis M, Kok CH, Bilardi RA, Sandow JJ, Silke N, Mason K, Visser J, Jabbour
560 AM, Glaser SP et al. 2013. HoxA9 regulated Bcl-2 expression mediates survival of
561 myeloid progenitors and the severity of HoxA9-dependent leukemia. *Oncotarget* **4**: 1933-
562 1947.
563 Carpentieri JA, Di Cicco A, Lampic M, Andreau D, Del Maestro L, El Marjou F, Coquand L,
564 Bahi-Buisson N, Brault JB, Baffet AD. 2022. Endosomal trafficking defects alter neural
565 progenitor proliferation and cause microcephaly. *Nat Commun* **13**: 16.
566 Castets F, Rakitina T, Gaillard S, Moqrich A, Mattei MG, Monneron A. 2000. Zinedin, SG2NA,
567 and striatin are calmodulin-binding, WD repeat proteins principally expressed in the brain.
568 *J Biol Chem* **275**: 19970-19977.
569 Chen YH, Huang TY, Lin YT, Lin SY, Li WH, Hsiao HJ, Yan RL, Tang HW, Shen ZQ, Chen GC
570 et al. 2021. VPS34 K29/K48 branched ubiquitination governed by UBE3C and TRABID
571 regulates autophagy, proteostasis and liver metabolism. *Nat Commun* **12**: 1322.
572 Clague MJ, Urbe S, Komander D. 2019. Breaking the chains: deubiquitylating enzyme specificity
573 begets function. *Nat Rev Mol Cell Biol*.
574 Creuzet SE, Martinez S, Le Douarin NM. 2006. The cephalic neural crest exerts a critical effect
575 on forebrain and midbrain development. *Proc Natl Acad Sci U S A* **103**: 14033-14038.
576 Deciphering Developmental Disorders S. 2015. Large-scale discovery of novel genetic causes of
577 developmental disorders. *Nature* **519**: 223-228.
578 Dickinson ME, Flenniken AM, Ji X, Teboul L, Wong MD, White JK, Meehan TF, Weninger WJ,
579 Westerberg H, Adissu H et al. 2016. High-throughput discovery of novel developmental
580 phenotypes. *Nature* **537**: 508-514.
581 Dogterom M, Koenderink GH. 2019. Actin-microtubule crosstalk in cell biology. *Nat Rev Mol*
582 *Cell Biol* **20**: 38-54.
583 Efimova N, Yang C, Chia JX, Li N, Lengner CJ, Neufeld KL, Svitkina TM. 2020. Branched actin
584 networks are assembled on microtubules by adenomatous polyposis coli for targeted
585 membrane protrusion. *J Cell Biol* **219**.

586 Erpapazoglou Z, Walker O, Haguenauer-Tsapis R. 2014. Versatile roles of k63-linked ubiquitin
587 chains in trafficking. *Cells* **3**: 1027-1088.
588 Hamada F, Bienz M. 2002. A Drosophila APC tumour suppressor homologue functions in cellular
589 adhesion. *Nat Cell Biol* **4**: 208-213.
590 Harris LD, Le Pen J, Scholz N, Mieszczanek J, Vaughan N, Davis S, Berridge G, Kessler BM,
591 Bienz M, Licchesi JDF. 2021. The deubiquitinase TRABID stabilizes the K29/K48-
592 specific E3 ubiquitin ligase HECTD1. *J Biol Chem* **296**: 100246.
593 Hjerpe R, Aillet F, Lopitz-Otsoa F, Lang V, England P, Rodriguez MS. 2009. Efficient protection
594 and isolation of ubiquitylated proteins using tandem ubiquitin-binding entities. *EMBO Rep*
595 **10**: 1250-1258.
596 Hwang J, Pallas DC. 2014. STRIPAK complexes: structure, biological function, and involvement
597 in human diseases. *Int J Biochem Cell Biol* **47**: 118-148.
598 Komander D, Clague MJ, Urbe S. 2009. Breaking the chains: structure and function of the
599 deubiquitinases. *Nat Rev Mol Cell Biol* **10**: 550-563.
600 Kounatidis I, Chtarbanova S, Cao Y, Hayne M, Jayanth D, Ganetzky B, Ligoxygakis P. 2017. NF-
601 kappaB Immunity in the Brain Determines Fly Lifespan in Healthy Aging and Age-Related
602 Neurodegeneration. *Cell Rep* **19**: 836-848.
603 Kristariyanto YA, Abdul Rehman SA, Campbell DG, Morrice NA, Johnson C, Toth R, Kulathu
604 Y. 2015. K29-selective ubiquitin binding domain reveals structural basis of specificity and
605 heterotypic nature of k29 polyubiquitin. *Mol Cell* **58**: 83-94.
606 Kuck U, Radchenko D, Teichert I. 2019. STRIPAK, a highly conserved signaling complex,
607 controls multiple eukaryotic cellular and developmental processes and is linked with
608 human diseases. *Biol Chem* **400**: 1005-1022.
609 Lahav-Ariel L, Caspi M, Nadar-Ponniah PT, Zelikson N, Hofmann I, Hanson KK, Franke WW,
610 Sklan EH, Avraham KB, Rosin-Arbesfeld R. 2019. Striatin is a novel modulator of cell
611 adhesion. *FASEB J* **33**: 4729-4740.
612 Leto DE, Morgens DW, Zhang L, Walczak CP, Elias JE, Bassik MC, Kopito RR. 2019. Genome-
613 wide CRISPR Analysis Identifies Substrate-Specific Conjugation Modules in ER-
614 Associated Degradation. *Mol Cell* **73**: 377-389 e311.
615 Licchesi JD, Mieszczanek J, Mevissen TE, Rutherford TJ, Akutsu M, Virdee S, El Oualid F, Chin
616 JW, Ovaa H, Bienz M et al. 2012. An ankyrin-repeat ubiquitin-binding domain determines

617 TRABID's specificity for atypical ubiquitin chains. *Nature structural & molecular biology*
618 **19**: 62-71.
619 Madsen CD, Hooper S, Tozluoglu M, Bruckbauer A, Fletcher G, Erler JT, Bates PA, Thompson
620 B, Sahai E. 2015. STRIPAK components determine mode of cancer cell migration and
621 metastasis. *Nat Cell Biol* **17**: 68-80.
622 Matsuda W, Furuta T, Nakamura KC, Hioki H, Fujiyama F, Arai R, Kaneko T. 2009. Single
623 nigrostriatal dopaminergic neurons form widely spread and highly dense axonal
624 arborizations in the neostriatum. *J Neurosci* **29**: 444-453.
625 Nathke IS, Adams CL, Polakis P, Sellin JH, Nelson WJ. 1996. The adenomatous polyposis coli
626 tumor suppressor protein localizes to plasma membrane sites involved in active cell
627 migration. *J Cell Biol* **134**: 165-179.
628 Neisch AL, Neufeld TP, Hays TS. 2017. A STRIPAK complex mediates axonal transport of
629 autophagosomes and dense core vesicles through PP2A regulation. *J Cell Biol* **216**: 441-
630 461.
631 Ng SS, De Labastida Rivera F, Yan J, Corvino D, Das I, Zhang P, Kuns R, Chauhan SB, Hou J,
632 Li XY et al. 2020. The NK cell granule protein NKG7 regulates cytotoxic granule
633 exocytosis and inflammation. *Nat Immunol* **21**: 1205-1218.
634 Preitner N, Quan J, Nowakowski DW, Hancock ML, Shi J, Tcherkezian J, Young-Pearse TL,
635 Flanagan JG. 2014. APC is an RNA-binding protein, and its interactome provides a link to
636 neural development and microtubule assembly. *Cell* **158**: 368-382.
637 Rosin-Arbesfeld R, Ihrke G, Bienz M. 2001. Actin-dependent membrane association of the APC
638 tumour suppressor in polarized mammalian epithelial cells. *EMBO J* **20**: 5929-5939.
639 Sakuma C, Kawauchi T, Haraguchi S, Shikanai M, Yamaguchi Y, Gelfand VI, Luo L, Miura M,
640 Chihara T. 2014. Drosophila Strip serves as a platform for early endosome organization
641 during axon elongation. *Nat Commun* **5**: 5180.
642 Sakuma C, Okumura M, Umehara T, Miura M, Chihara T. 2015. A STRIPAK component Strip
643 regulates neuronal morphogenesis by affecting microtubule stability. *Sci Rep* **5**: 17769.
644 Sarkar AA, Zohn IE. 2012. Hectd1 regulates intracellular localization and secretion of Hsp90 to
645 control cellular behavior of the cranial mesenchyme. *J Cell Biol* **196**: 789-800.
646 Shih PY, Lee SP, Chen YK, Hsueh YP. 2014. Cortactin-binding protein 2 increases microtubule
647 stability and regulates dendritic arborization. *J Cell Sci* **127**: 3521-3534.

648 Silva CG, Peyre E, Nguyen L. 2019. Cell migration promotes dynamic cellular interactions to
649 control cerebral cortex morphogenesis. *Nat Rev Neurosci* **20**: 318-329.
650 Sowa ME, Bennett EJ, Gygi SP, Harper JW. 2009. Defining the human deubiquitinating enzyme
651 interaction landscape. *Cell* **138**: 389-403.
652 Thompson LH, Parish CL. 2013. Transplantation of fetal midbrain dopamine progenitors into a
653 rodent model of Parkinson's disease. *Methods Mol Biol* **1059**: 169-180.
654 Tran H, Bustos D, Yeh R, Rubinfeld B, Lam C, Shriver S, Zilberleyb I, Lee MW, Phu L, Sarkar
655 AA et al. 2013. HectD1 E3 ligase modifies adenomatous polyposis coli (APC) with
656 polyubiquitin to promote the APC-axin interaction. *J Biol Chem* **288**: 3753-3767.
657 Tran H, Hamada F, Schwarz-Romond T, Bienz M. 2008. Trabid, a new positive regulator of Wnt-
658 induced transcription with preference for binding and cleaving K63-linked ubiquitin
659 chains. *Genes Dev* **22**: 528-542.
660 Tran H, Polakis P. 2012. Reversible modification of adenomatous polyposis coli (APC) with K63-
661 linked polyubiquitin regulates the assembly and activity of the beta-catenin destruction
662 complex. *J Biol Chem* **287**: 28552-28563.
663 Vaughan N, Scholz N, Lindon C, Licchesi JDF. 2022. The E3 ubiquitin ligase HECTD1
664 contributes to cell proliferation through an effect on mitosis. *Sci Rep* **12**: 13160.
665 Vega-Lopez GA, Cerrizuela S, Tribulo C, Aybar MJ. 2018. Neurocristopathies: New insights 150
666 years after the neural crest discovery. *Dev Biol* **444 Suppl 1**: S110-S143.
667 Yokota Y, Kim WY, Chen Y, Wang X, Stanco A, Komuro Y, Snider W, Anton ES. 2009. The
668 adenomatous polyposis coli protein is an essential regulator of radial glial polarity and
669 construction of the cerebral cortex. *Neuron* **61**: 42-56.
670 Yu Y, Zheng Q, Erramilli SK, Pan M, Park S, Xie Y, Li J, Fei J, Kossiakoff AA, Liu L et al. 2021.
671 K29-linked ubiquitin signaling regulates proteotoxic stress response and cell cycle. *Nat*
672 *Chem Biol* **17**: 896-905.
673 Yuan WC, Lee YR, Lin SY, Chang LY, Tan YP, Hung CC, Kuo JC, Liu CH, Lin MY, Xu M et
674 al. 2014. K33-Linked Polyubiquitination of Coronin 7 by Cul3-KLHL20 Ubiquitin E3
675 Ligase Regulates Protein Trafficking. *Mol Cell* **54**: 586-600.
676
677

678 **Figures**

679 **Figure 1. Trabid patient mutants are impaired in DUB activity and STRIPAK binding.**

680 **A**. Trabid patient mutations R438W and A451V flank either side of the catalytic cysteine C443

681 in Trabid's AnkOTU domain.

682 **B**. Residue R438 project prominently into the catalytic cleft formed by the Ank and OTU

683 domain, whereas residue A451 reside at the back of the active site. The positions of the catalytic

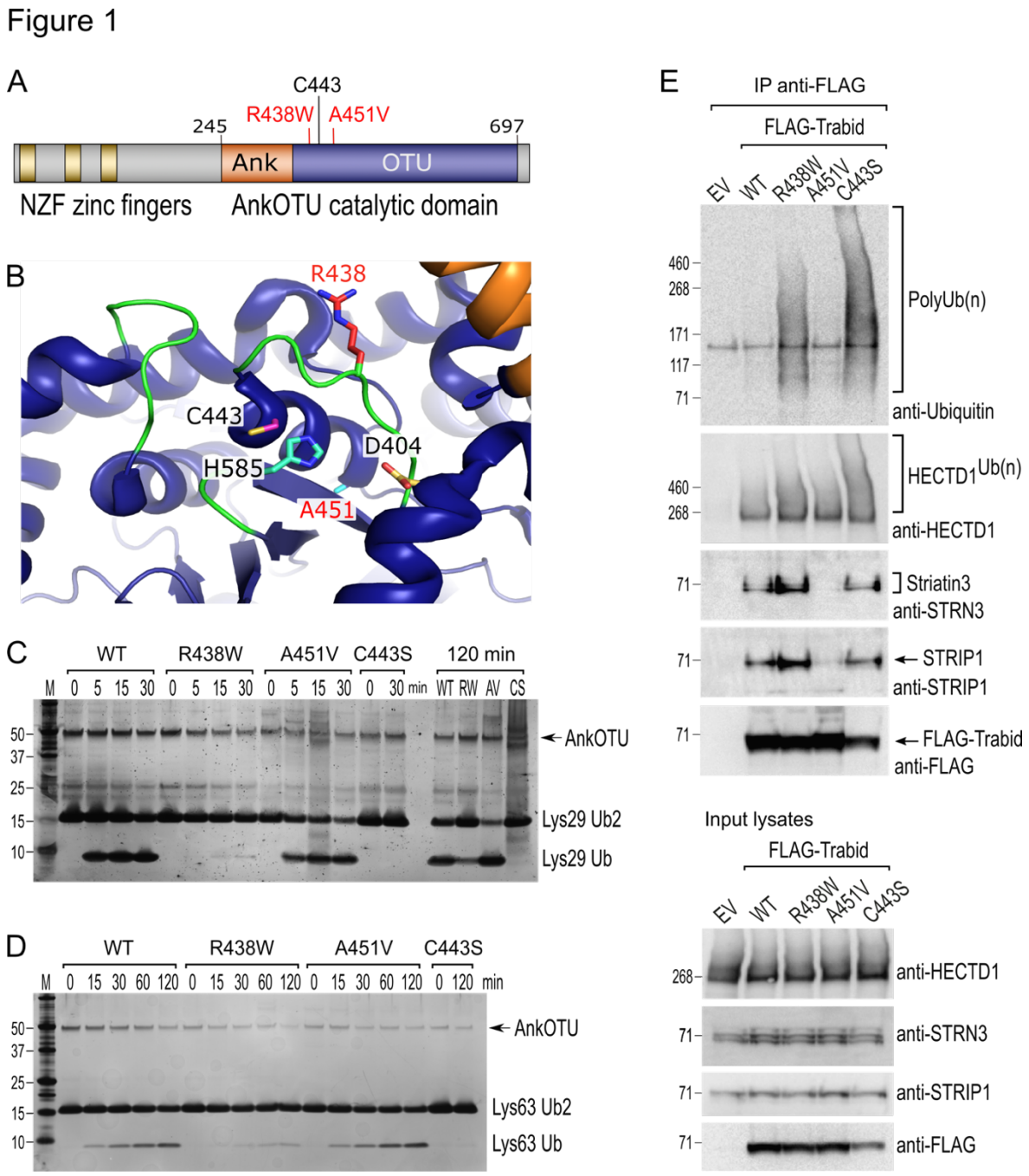

684 triad residues C443, H585 and D404 are shown. Crystal structure of AnkOTU domain: PDB
685 3ZRH.
686 **C** and **D**. *In vitro* DUB assays. Hydrolysis of Lys29-linked (C) and Lys63-linked (D) di-
687 ubiquitin chains by purified wild-type and mutant Trabid AnkOTU proteins. The Trabid R438W
688 AnkOTU domain exhibit strongly reduced DUB activity M, molecular weight markers in
689 kilodaltons.
690 **E**. Immunoprecipitation of FLAG-Trabid from the lysates of transfected HEK293T cells showed
691 that FLAG-Trabid R438W and C443S mutants co-precipitated high amounts of endogenous
692 polyubiquitin (PolyUb(n) smear), indicating impaired DUB activity. FLAG-Trabid A451V failed
693 to efficiently co-precipitate Striatin3 and STRIP1, indicating loss of binding to the STRIPAK
694 complex. All FLAG-Trabid proteins co-precipitated similar amounts of the E3 ubiquitin ligase
695 HECTD1. EV, empty vector control.
696
697
698
699
700
701
702
703
704
705
706
707
708
709

Figure 2

A

Knock-in mouse models

Zranb1$^{R438W/+}$ and *Zranb1*$^{A451V/+}$ (KI/+)

Zranb1$^{R438W/R438W}$ and *Zranb1*$^{A451V/A451V}$ (KI/KI)

B

Observed number of mice of all genotypes

	+/+	KI/+	KI/KI
R438W colony (n=184)	59	89	36
Expected Mendelian 1:2:1 ratio	46	92	46
A451V colony (n=220)	50	101	69
Expected Mendelian 1:2:1 ratio	55	110	55

C

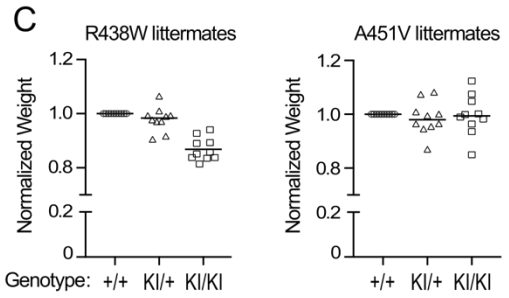

D

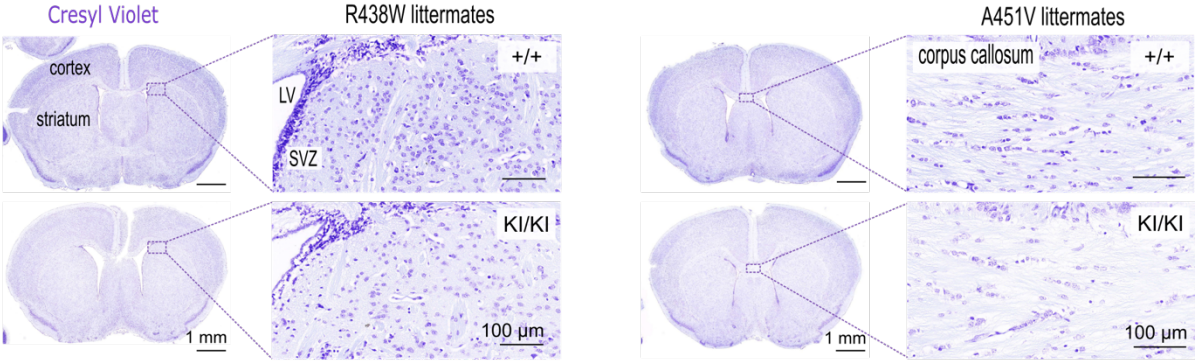

E

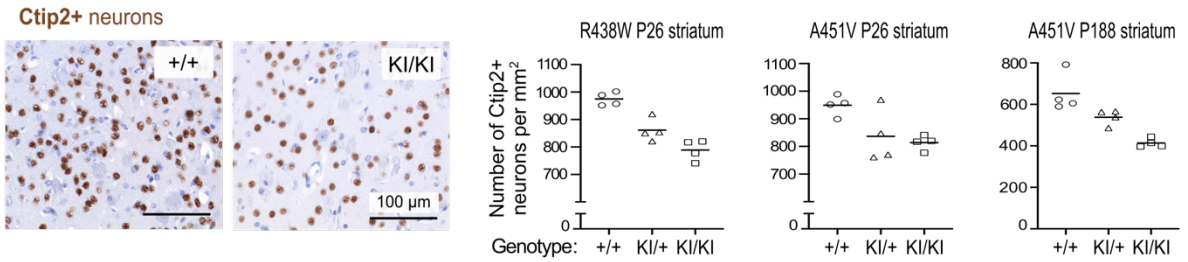

F

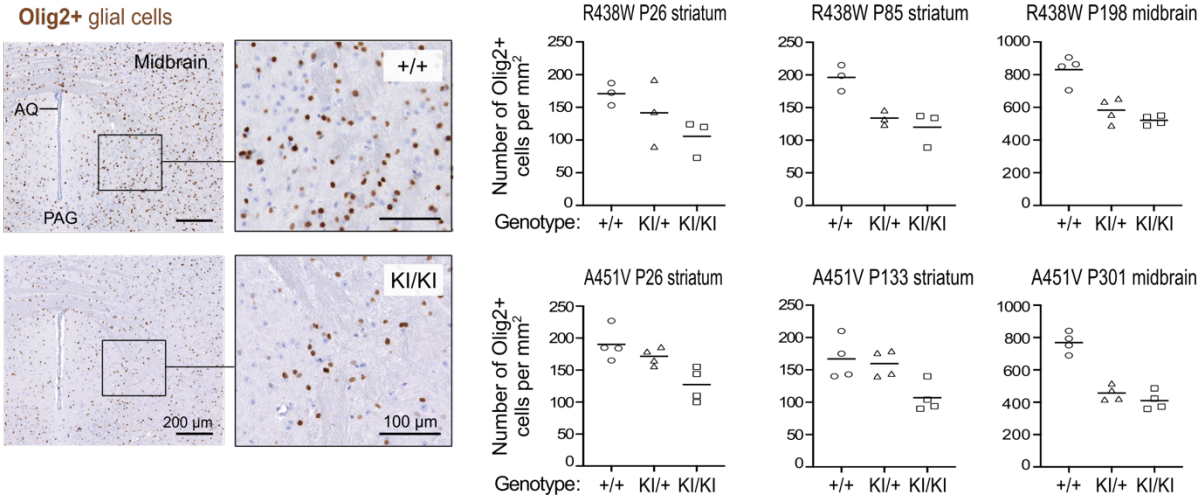

710

711 **Figure 2. Decreased cell density in the brains of mice harbouring Trabid patient mutations.**
712 **A**. Schematic of knock-in mouse strains harbouring *Zranb1/Trabid* patient mutations generated
713 by CRISPR/Cas9 genome editing.
714 **B**. Numbers of mice of all genotypes produced from heterozygous intercrosses in the R438W or
715 A451V colony, respectively.
716 **C**. Normalized weight of 10 sets of weaned littermate mice (5 males, 5 females; age range P26-
717 P222) from each Trabid mutant colony. For each set of littermates, the weight of the wild-type
718 (+/+) mouse was set at 1 and the weight of KI/+ or KI/KI mutant mice expressed as a ratio of the
719 wild-type mouse weight.
720 **D**. Coronal brain sections (Bregma ±0.3mm) of weaned (postnatal day P26) littermate males
721 from the R438W and A451V mouse colonies were stained with Cresyl Violet to assess general
722 anatomy and cellular organisation in the cerebral cortex and striatum. LV, lateral ventricle; SVZ,
723 subventricular zone. An overall decrease in Cresyl Violet staining intensity was evident in
724 mutant homozygous (KI/KI) sections from both mouse strains compared to similar sections from
725 the respective wild-type (+/+) littermate.
726 **E**. Ctip2 IHC revealed reduced numbers of medium spiny neurons in the striatum of mutant mice
727 from the R438W and A451V colonies compared to wild-type littermate mice. Representative
728 images shown are coronal brain sections of P26 male littermates from the R438W colony. Each
729 data point represents the cell count in a randomly selected, non-overlapping 1 mm square area in
730 the striatum from both brain hemispheres. The age and brain region of the cell count for 3 sets of
731 littermate mice from the indicated mutant strain are specified. Cell numbers were quantified
732 blinded to genotype using images processed in Fiji software. See Supplementary Figure 2.
733 **F.** Olig2 IHC revealed reduced numbers of oligodendrocytes in the striatum and midbrain of
734 homozygous mice from the R438W and A451V colonies compared to respective wild-type
735 littermates. Representative images shown are coronal sections from the ventral midbrain of P301
736 female littermates from the A451V colony (AQ, cerebral aqueduct; PAQ, periaqueductal gray).
737 Each data point represents the cell count in a randomly selected, non-overlapping 1 mm square
738 area in the striatum or midbrain from both brain hemispheres. The age and brain region of the
739 cell count for 3 sets of littermate mice from the indicated mutant strain are specified. Cell
740 numbers were quantified blinded to genotype using images processed in Fiji. See Supplementary
741 Figure 2.

Figure 3

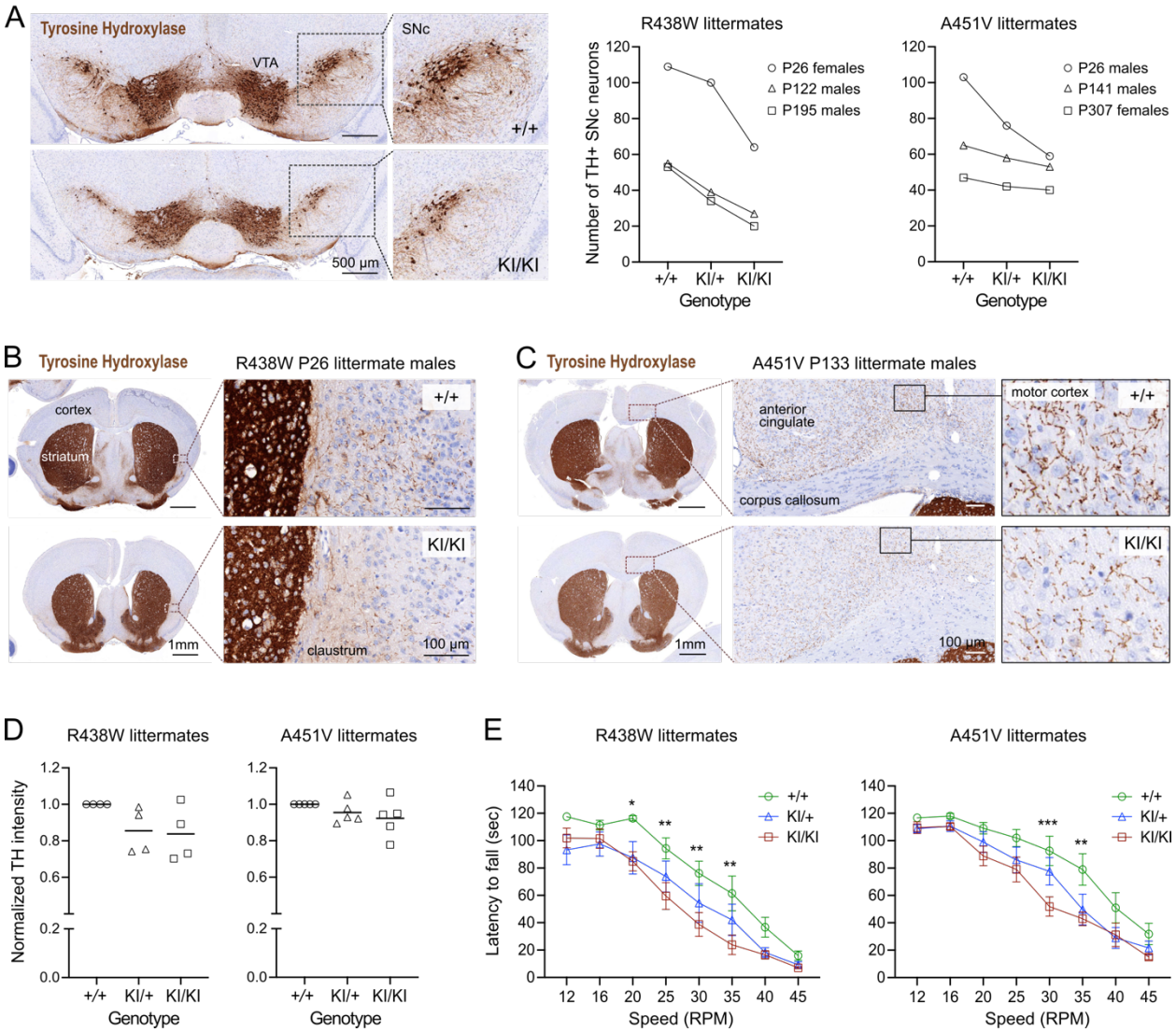

Figure 3. Trabid mutant mice exhibited a motor deficit consistent with reduced numbers of dopaminergic neurons and projections.

A. Tyrosine Hydroxylase (TH) IHC of coronal midbrain sections revealed reduced numbers of TH+ dopaminergic neurons in the substantia nigra pars compacta (SNc) of homozygous mutant mice from the Trabid R438W and A451V colonies compared to similar midbrain sections of the respective wild-type littermates. Representative images shown are midbrain sections of P26 female littermates from the R438W colony. VTA, ventral tegmental area. Numbers of TH+ SNc neurons were quantified using IHC images processed in Fiji. See Supplementary Figure 2.

752 **B**. Tyrosine Hydroxylase IHC of coronal brain sections (Bregma ±0.3mm) of P26 littermate
753 mice from the Trabid R438W colony revealed reduced TH staining intensity in the striatum and
754 fewer TH+ projections in the adjacent cortex of homozygous mutant mice compared to similar
755 regions in the wild-type littermate (magnified area).
756 **C**. Tyrosine Hydroxylase IHC of coronal brain sections (Bregma ±0.3mm) of P133 littermate
757 mice from the Trabid A451V colony revealed reduced abundance and intensity of TH+
758 projections in several cortical regions including the primary/secondary motor cortex of
759 homozygous mutant mice compared to similar regions in the wild-type littermate (magnified
760 area).
761 **D**. Tyrosine Hydroxylase staining intensity in the striatum of mutant mice from the R438W and
762 A451V colonies normalized to the staining intensity of wild-type littermate sections. IHC signals
763 were measured as the optical density of the region of interest demarcated manually using Fiji.
764 Each symbol represents one mouse of the indicated genotype belonging to a set of littermate
765 mice from the R438W colony (n=4 sets: P26 males, P93 females, P307 males, P480 females) or
766 the A451V colony (n=5 sets: P26 males, P41 females, P133 males, P188 females, P303 females).
767 **E**. Rotarod performance of 3 to 4-month-old littermate mice from the R438W and A451V
768 colonies. Each data point represents the average latencies of 8 mice (4 males, 4 females), where
769 each mouse was subjected to 6 trials over 3 days. Wild-type (+/+), heterozygous (KI/+) and
770 homozygous (KI/KI) littermate mice were tested together. The experimenter was blinded to
771 genotype. A repeated measures two-way ANOVA and Dunnett's multiple comparisons test was
772 applied to the data, using wild-type mice as the control group. Asterisks denote statistically
773 significant differences between wild-type (+/+) and homozygous (KI/KI) mutant mice. *$p<0.05$,
774 **$p<0.01$, ***$p<0.001$. Error bars, ±SEM.
775
776
777
778
779
780
781

Figure 4

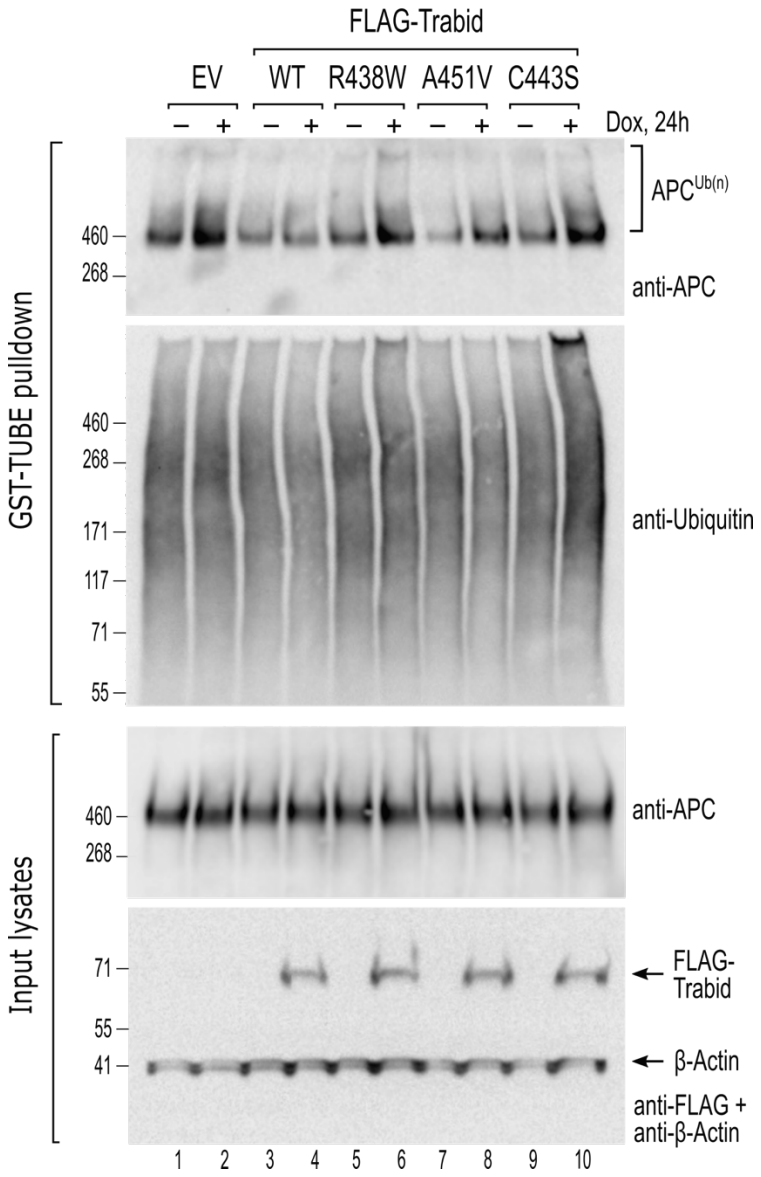

Figure 4. Trabid patient mutants fail to efficiently suppress APC ubiquitylation in cells. HEK293 cells stably transfected with doxycycline inducible constructs for the expression of wild-type or mutant FLAG-Trabid were untreated (-) or treated with dox (+; 100 ng/ml) for 24h. Cell lysates were subjected to a GST-TUBE pulldown to enrich the ubiquitylated proteome. Precipitated material and input lysates were processed for Western blotting using the indicated antibodies. Endogenous APC protein levels remained unchanged irrespective of FLAG-Trabid expression (input lysates), but ubiquitylated APC species were only efficiently suppressed by wild-type FLAG-Trabid expression ($APC^{Ub(n)}$; WT +). EV, empty vector control.

Figure 5

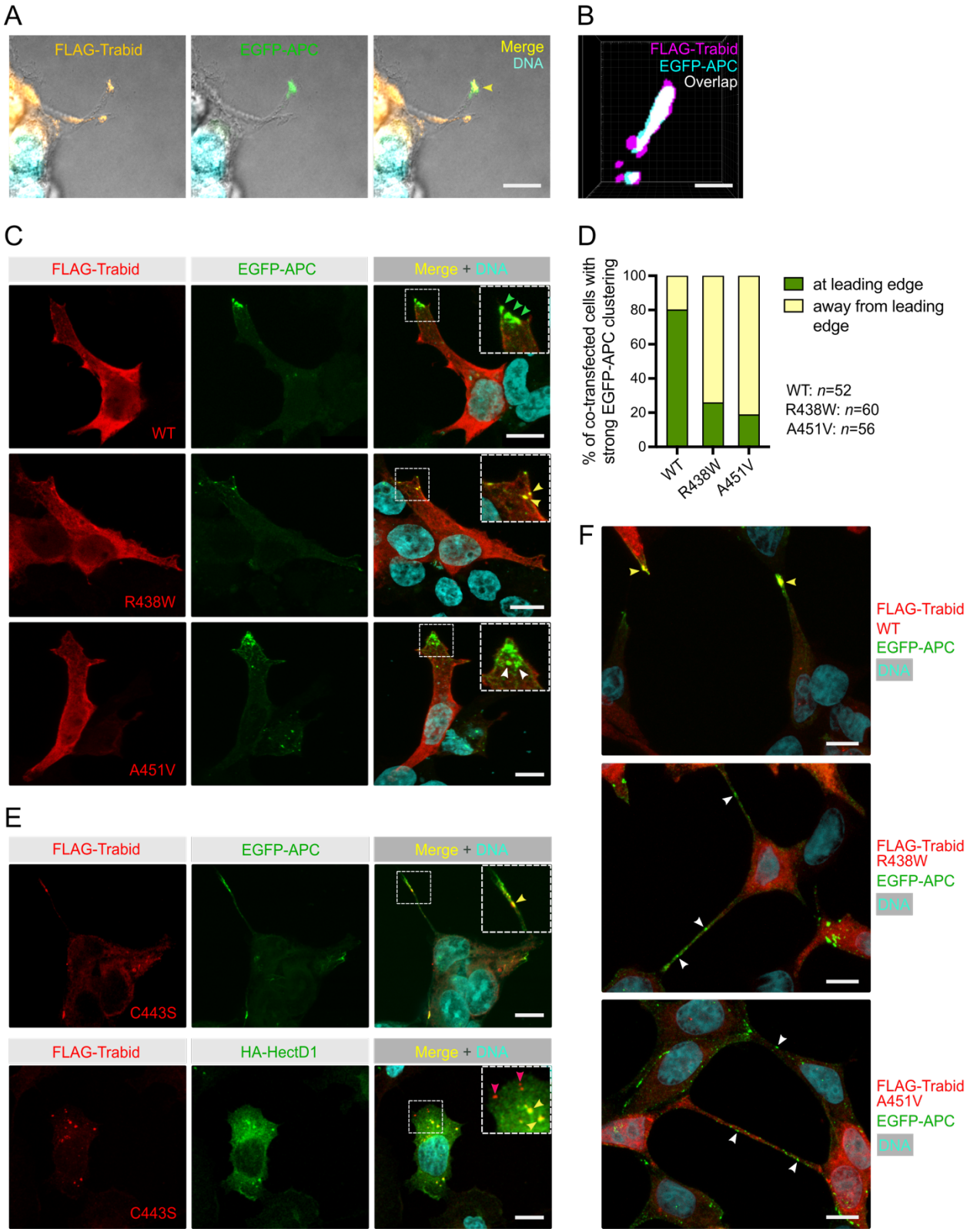
A
FLAG-Trabid
EGFP-APC
Merge
DNA
B
FLAG-Trabid
EGFP-APC
Overlap
C
FLAG-Trabid
EGFP-APC
Merge + DNA
WT
R438W
A451V
D
% of co-transfected cells with strong EGFP-APC clustering
100
80
60
40
20
0
WT
R438W
A451V
at leading edge
away from leading edge
WT: n=52
R438W: n=60
A451V: n=56
E
FLAG-Trabid
EGFP-APC
Merge + DNA
C443S
FLAG-Trabid
HA-HectD1
Merge + DNA
C443S
F
FLAG-Trabid
WT
EGFP-APC
DNA
FLAG-Trabid
R438W
EGFP-APC
DNA
FLAG-Trabid
A451V
EGFP-APC
DNA

792

793 **Figure 5. Trabid patient mutants impede the transport of EGFP-APC to the leading edge**
794 **of migrating cells.**
795 **A**. Combined differential interference contrast and immunofluorescence images of HEK293T
796 cells extending long cell processes that contain FLAG-Trabid and EGFP-APC in the cortical
797 protrusions of co-transfected cells (arrowhead in merged image). Scale bar, 10 μm.
798 **B**. 3D-SIM super resolution microscopy analysis of HEK293T cell tip clusters (n=5) revealed
799 ~30% overlap of FLAG-Trabid and EGFP-APC signals at resolutions of ~100 nm in *xy* and 320
800 nm in *z*. Scale bar, 100 nm.
801 **C**. EGFP-APC membrane clusters at the leading edge of migrating HEK293T cells (green
802 arrowheads) are readily detected with FLAG-Trabid wild-type co-expression. In cells expressing
803 FLAG-Trabid patient mutants, EGFP-APC aggregate in punctate structures near the leading edge
804 (white arrowheads), that are often sequestered together with the FLAG-Trabid R438W mutant
805 (yellow arrowheads). Scale bar, 10 μm.
806 **D**. Quantification of strong EGFP-APC clustering at or away from the leading edge membrane of
807 co-transfected HEK293T cells, as shown in C. Numbers of cells analysed from 3 independent
808 transfections are shown.
809 **E**. In co-transfected HEK293T cells, DUB-dead FLAG-Trabid C443S form punctae that
810 sequesters EGFP-APC near the tips of long cell protrusions or sequesters HA-HECTD1 in the
811 cytoplasm (yellow arrowheads). Notably, HA-HECTD1 was not detected in FLAG-Trabid
812 C443S punctae that form near the leading edge membrane of migrating cells (red arrowheads).
813 Scale bar, 10 μm.
814 **F**. In near-confluent HEK293T cells 48h post transfection, FLAG-Trabid patient mutants induce
815 long thin tubes that connect neigbouring cells. Extensive EGFP-APC aggregations are
816 conspicuous along these tubular structures. Scale bar, 10 μm.
817
818
819
820
821
822
823

Figure 6

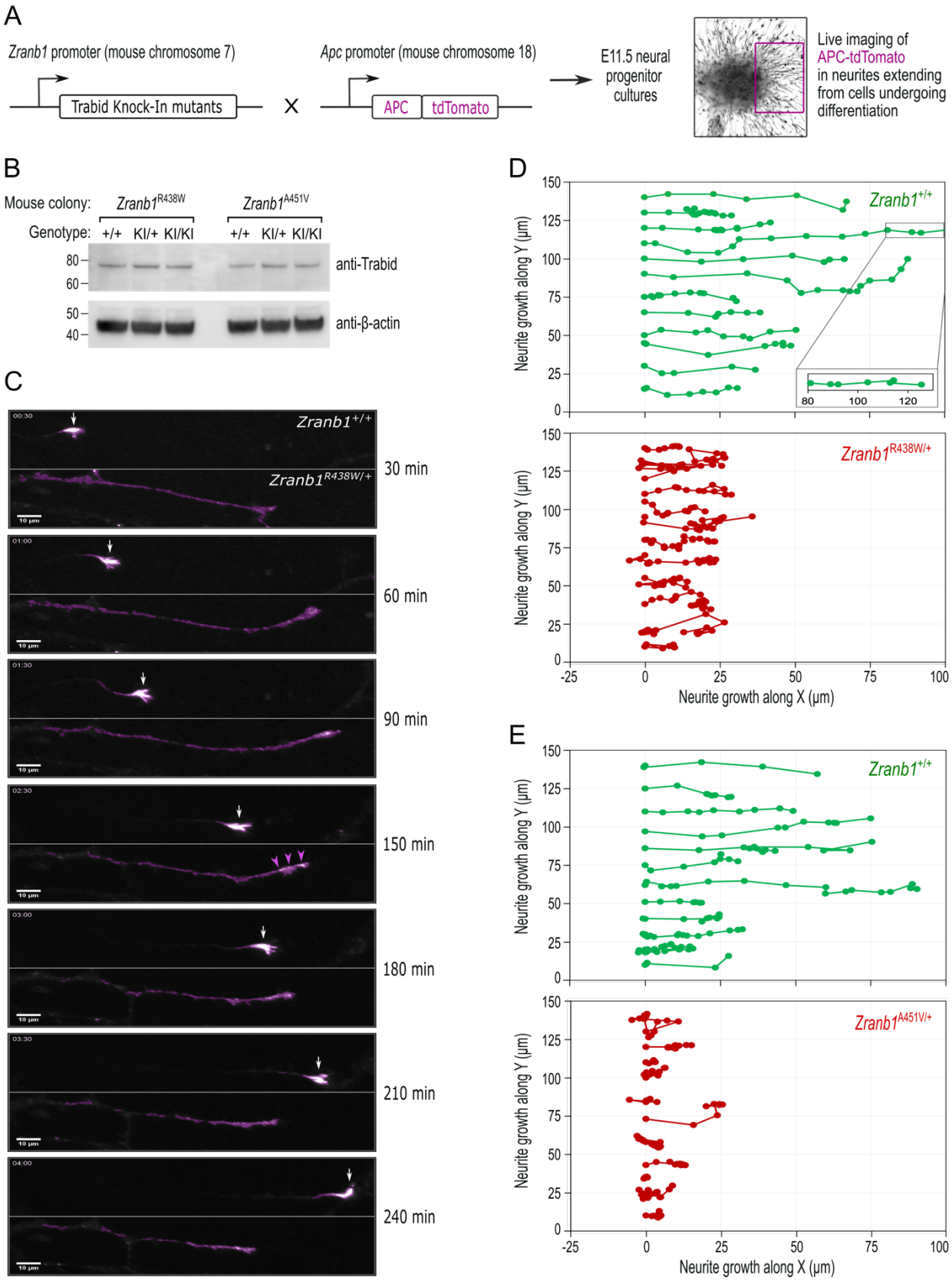
A
Zranb1 promoter (mouse chromosome 7)
Trabid Knock-In mutants
X
Apc promoter (mouse chromosome 18)
APC
tdTomato
E11.5 neural progenitor cultures
Live imaging of APC-tdTomato in neurites extending from cells undergoing differentiation
B
Mouse colony:
Zranb1R438W
Zranb1A451V
Genotype:
+/+ KI/+ KI/KI
+/+ KI/+ KI/KI
80
60
50
40
anti-Trabid
anti-β-actin
C
Zranb1+/+
Zranb1R438W/+
30 min
60 min
90 min
150 min
180 min
210 min
240 min
D
Zranb1+/+
Zranb1R438W/+
Neurite growth along Y (µm)
Neurite growth along X (µm)
E
Zranb1+/+
Zranb1A451V/+
Neurite growth along Y (µm)
Neurite growth along X (µm)

824

825 **Figure 6. Trabid patient mutations perturb the trafficking of APC-tdTomato and the**
826 **trajectory of neurite outgrowth.**
827 **A**. Schematic of outcross between knock-in mice harbouring *Zranb1/Trabid* patient mutations
828 and *Apc*^{tdTomato} mice, where the APC-tdTomato fluorescent protein is expressed under the control
829 of the endogenous *Apc* gene promoter. Midbrain neural progenitors derived from E11.5 embryos
830 of these outcrosses were used for live cell imaging of APC-tdTomato trafficking in growing
831 neurites.
832 **B**. Western blot analysis of Trabid protein expression in E11.5 midbrain neural progenitors
833 derived from heterozygous intercrosses in the *Zranb1/Trabid* R438W or A451V mouse colonies.
834 Mutant Trabid protein levels are expressed at comparable levels to wild-type Trabid protein
835 (compare KI/KI to +/+).
836 **C**. Live cell imaging of APC-tdTomato in neurites extending from E11.5 midbrain neural
837 progenitors of a *Zranb1*$^{R438W/+}$;*Apc*$^{tdTom/+}$ outcross. The frames shown are from a 4h time lapse
838 portraying the movement of APC-tdTomato. APC-tdTomato accumulated in the tips of neurites
839 with wild-type Trabid (*Zranb1*$^{+/+}$) to generate growth cones that drive axon elongation (white
840 arrows). In neurons with mutant Trabid (*Zranb1*$^{\mathrm{R438W/+}}$; *Zranb1*$^{\mathrm{A451V/+}}$ data not shown), APC-
841 tdTomato intensities were broadly distributed along neurites (purple arrowheads) and the
842 formation of growth cones was abrogated. Scale bar, 10 μm.
843 **D** and **E**. The movement of Apc-tdTomato in individual neurite tips was tracked to visualize
844 growth trajectory. Neurites extending from E11.5 midbrain neural progenitors of
845 *Zranb1*$^{R438W/+}$;*Apc*$^{tdTom/+}$ (D) or *Zranb1*$^{A451V/+}$;*Apc*$^{tdTom/+}$ (E) outcrosses were analysed. Each data
846 point represents the location of APC-tdTomato at 15-min intervals of a 4h time lapse. APC-
847 tdTomato fluorescence synchronised with the movement of a membrane dye during neurite
848 extension/retraction (data not shown) and was therefore used as a proxy for neurite growth along
849 an arbitrary X and Y plane. Neurite tracking data were compiled from the imaging of neurite
850 outgrowth in 3 independent neurosphere cultures established from E11.5 embryos of 3
851 independent *Zranb1*$^{R438W/+}$;*Apc*$^{tdTom/+}$ or *Zranb1*$^{A451V/+}$;*Apc*$^{tdTom/+}$ outcrosses. All image
852 acquisition, processing and analyses were performed blinded to genotype.
853
854
855

Figure 7

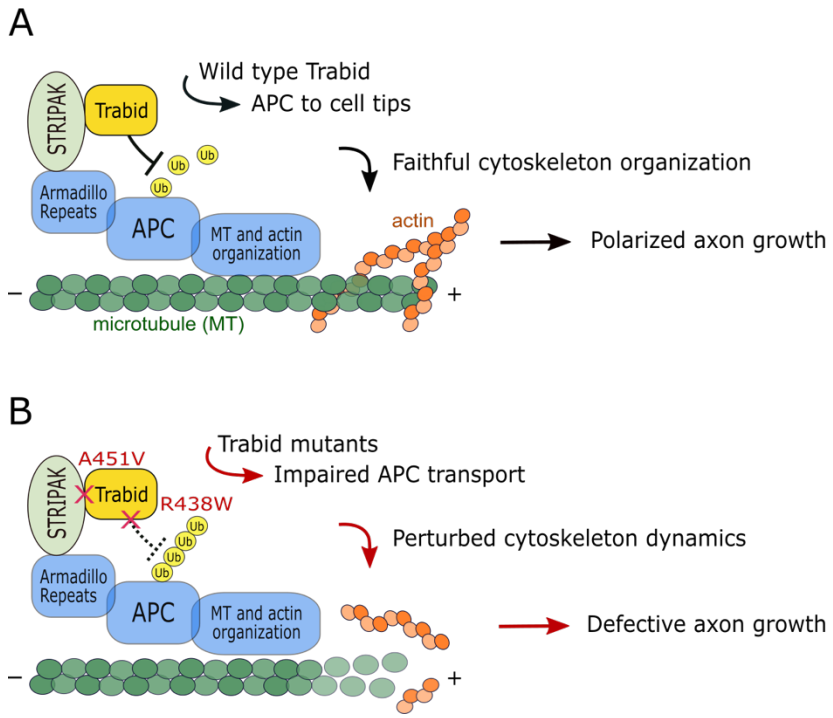

Figure 7. Model of Trabid's mechanism of action in axon growth and guidance.

A. STRIPAK recruits Trabid to deubiquitylate APC (and possibly other substrates). This promotes efficient APC accumulation at microtubule plus ends to coordinate the actin and microtubule cytoskeleton dynamics that drive directional cell migration and polarised axon growth.

B. In cells expressing Trabid mutants that are DUB-impaired (R438W) or STRIPAK-binding-deficient (A451V), APC becomes persistently modified with ubiquitin chains that retard its transport to cell tips. This impairs cytoskeleton organisation which leads to defective axon elongation and cell migration. Future studies will aim to identify the mechanism of Trabid recruitment to STRIPAK, the ubiquitin-modified residue(s) on APC (and possibly other substrates), and the composition of polyubiquitin linkages on substrates including the Lys29- and Lys33-linked atypical chain types preferentially targeted by Trabid.